

Using Carrier Fringes to Study the High Temperature Deformation Behavior of a BGA Package Under Extended Dwell Times

K.R. Tunga · S.K. Sitaraman

Received: 11 May 2007 / Accepted: 10 December 2007 / Published online: 8 January 2008
© Society for Experimental Mechanics 2007

Abstract There is a compelling need to experimentally understand solder joint deformation behavior at high temperatures over an extended period of time. Accordingly, the deformation behavior of solder joints in a Ceramic Ball Grid Array (CBGA) package mounted on an organic FR4 board under extended dwell time at a high temperature has been studied using laser moiré interferometry. The warpage and the in-plane horizontal deformation of the ceramic substrate and the organic board as a function of time were determined. The variation of the normal strains and shear strains in the solder joints with time were also investigated. It was found that increased sensitivity was necessary to accurately determine the strains in the small sized solder joints. A new method utilizing carrier fringes to increase the sensitivity of the moiré interferometry system is proposed and has been used to determine the strains in the small sized solder joints. Increased sensitivity can be obtained merely by changing the incident angle of the laser light on the surface of the specimen, thereby making it unnecessary to use expensive phase shifting apparatus with the traditional laser moiré system.

Keywords High temperature dwell · Laser moiré interferometry · Carrier fringes · Ceramic Ball Grid Array package · Fourier transform

K.R. Tunga · S.K. Sitaraman (✉)
Computer Aided Simulation for Packaging Reliability (CASPaR)
Laboratory, The George W. Woodruff School of Mechanical
Engineering, Georgia Institute of Technology,
Atlanta, GA 30332-0405, USA
e-mail: suresh.sitaraman@me.gatech.edu

K.R. Tunga
e-mail: gtg958b@mail.gatech.edu

Nomenclature

U	displacement in the horizontal direction
V	displacement in the vertical direction
N_x	fringe order in the U field moiré pattern
N_y	fringe order in the V field moiré pattern
f	frequency of the virtual reference grating
λ	wavelength of the laser light used
α	incident angle for the coherent beam
f_s	frequency of the cross-line grating
ϵ_{yy}	total measured strain in the vertical direction
ϵ_{xy}	total measured shear strain
Δx	width of the solder ball
Δy	height of the solder ball
I	intensity of the fringe pattern as recorded in the CCD camera
I_{α}	intensity of fringe pattern from CCD camera after introducing carrier fringes, $\alpha=u$ for U field and $\alpha=v$ for V field
I_b	intensity due to background illumination
I_n	intensity due to background noise
I_o	intensity of the fringe pattern amplitude
Φ_{α}	phase of the fringe pattern. $\alpha=u$ for U field and $\alpha=v$ for V field
f_{cy}	frequency of the carrier fringes in the V field
f_{cx}	frequency of the carrier fringes in the U field
I_{α}	Intensity of the fringe pattern after introducing increasing the sensitivity. $\alpha=u$ for U field and $\alpha=v$ for V field
n	sensitivity factor

Background

Microelectronic packages used in several applications experience high temperature dwell over an extended period of time



lasting several hours. The high temperature dwell can be either due to operating surroundings (as in automotive and aerospace applications) or due to continued operation of the package (as in server applications). However, most of the experimental studies [1–3] have focused either on solder deformation behavior during high temperature dwell lasting less than 1 h or on long duration dwell at room temperature. A combination of creep deformation behavior of the solder joints at a high temperature and for a long duration has not been performed and should therefore be studied.

Laser moiré interferometry is a relatively new technique and has been used to find the in-plane deformation in microelectronic packages when subjected to thermal [4], mechanical [5], vibration [6] and electrical power loading [7]. A sensitivity as low as 417 nm/fringe order can be achieved by this method. When studying the deformation of the package as a whole, this sensitivity is sufficient. However, to obtain a more accurate deformation for small sized solder joints which exhibit higher strain gradients, higher fringe counting accuracy is needed. Various methods have been proposed to increase the fringe counting accuracy of the laser moiré interferometry system. Prominent among them are the immersion interferometer [8] and phase shifting technique [8–10] and phase based technique based on wavelet transforms [11]. When used in combination, these methods have the capability to increase the fringe counting accuracy over ten-fold [12]. Immersion interferometer requires the whole interferometer to be immersed in a liquid, typically water. This prohibits performing in-situ measurements of the package deformation. Phase shifting technique involves moving the whole interferometer parallel to the surface of the specimen and obtaining phase shifted fringes between the existing fringes thus increasing the accuracy of fringe counting. This requires investing on expensive piezo-electric motors and actuators to perform the phase shifting process. Moreover, the phase shifting process is done in a finite time interval and might be affected in the presence of vibrations.

The present paper proposes a method which uses carrier fringes to increase the fringe counting accuracy of the moiré interferometric system. Carrier fringes have been used in the past to better interpret the deformation data and to extract more detailed information from the deformation fringes [13–15]. They have also been used to obtain the strains in the solder joints [16]. Carrier fringes are introduced by a tiny adjustment of the angle of the incident laser beam on the grating specimen [8] and have an effect of introducing a constant strain in the specimen. The deformation fringes from actual displacement are modulated by the artificially introduced carrier fringes. A Fourier transform of the modulated fringe pattern is tri-modal in nature [17]. This characteristic can be used to obtain the phase information from the deformation fringes. The accuracy of fringe

counting can then be easily increased utilizing the phase of the fringes. This method was used to study the normal and shear strains in the solder joints in a ceramic BGA package when exposed to 100°C for 24 h. Since, the solder joints act as an interconnect material coupling the ceramic BGA substrate and the PWB, the strains in the solder joints are directly related to the deformation of these two materials. Therefore, the warpage and the horizontal in-plane deformation of the substrate and the PWB were also studied.

Theory of Laser Moiré Interferometry

Moiré interferometry is an optical method which provides whole field contour maps of in-plane displacements. A schematic diagram of the setting used for moiré interferometry is shown in Fig. 1 [18] where coherent He–Ne laser beams are incident on the moiré grating having a cross-line pattern on the surface with a frequency of 1,200 lines/mm. Sensitivity as low as 417 nm per fringe order can be achieved with this setup.

Coherent beams A and B when incident on the grating create a virtual reference grating in their zone of intersection. When the specimen deforms, the grating also deforms with it. This deformed grating interacts with the virtual reference grating to produce the moiré interference pattern. The beams A and B when incident in the horizontal direction produces vertical fringes and these fringes are termed as U field fringes. Analogous beams when incident in the vertical direction would create another virtual reference grating which interacts with the second set of lines, perpendicular to the first one, to create the V field fringes.

The displacements can then be determined from the fringes using [19]:

$$U = \frac{N_x}{f}, \quad V = \frac{N_y}{f} \quad (1)$$

where, N_x and N_y are the fringe orders in the U and V field moiré patterns respectively. f is the frequency of virtual reference grating and is given by:

$$f = \frac{2}{\lambda} \sin \alpha \quad (2)$$

where λ is the wavelength of the laser light used for the coherent beam and α is the angle at which the coherent beam is incident. It should be noted that in moiré interferometry, the frequency of the virtual grating is related to the cross-line grating frequency using:

$$f_s = \frac{f}{2} \quad (3)$$

where f_s is the number of lines per millimeter length in the cross-line grating and is equal to 1,200 lines/mm.

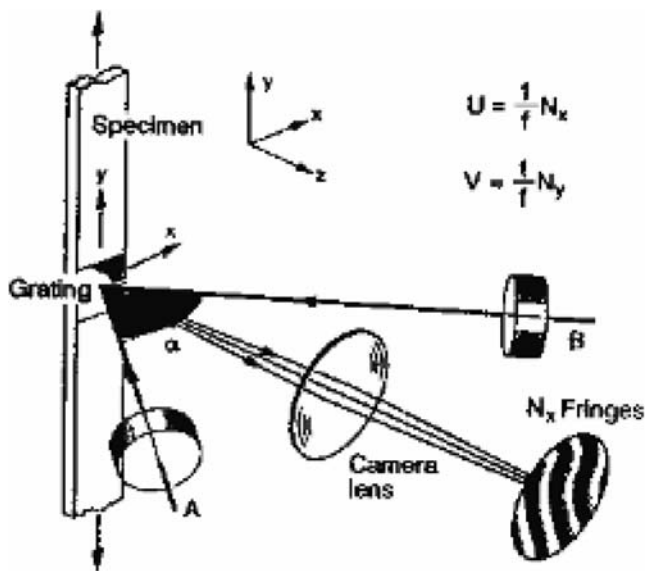
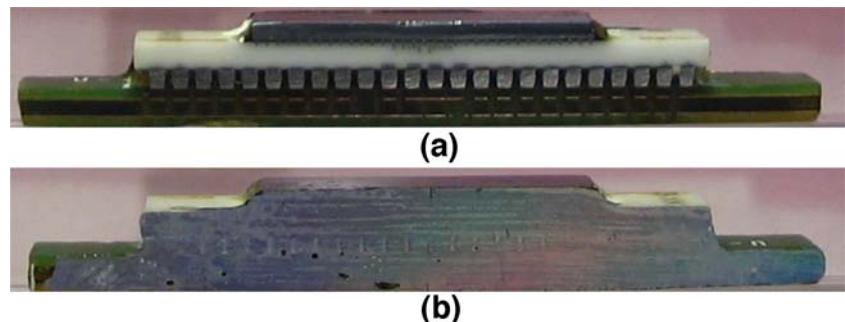


Fig. 1 Schematic of moiré interferometry [18]

Sample Preparation

The ceramic BGA package test vehicle assembly had more than 500 area array solder interconnects with 1 mm pitch. The solder interconnects consisted of high melting point alloy (90% Pb/10% Sn) and a eutectic solder fillet (63%Sn/37% Pb). The average standoff height of the solder interconnects was 0.817 mm. The ceramic BGA package consisted of a 15-mm underfilled flip-chip assembled on a 25-mm ceramic substrate. The thickness of the silicon chip and the ceramic substrate was 0.75 and 1.2 mm respectively. The ceramic BGA package was assembled onto a 1.75-mm thick FR4 board. The assembly was cut in the form of thin strips along a direction parallel to one of the sides of the square package. The cross-sectioned strip included four rows of solder balls. The strip was then ground and polished so as to expose one row of solder balls such that the plane of cut was along the center of the solder ball row. Grating, with 1,200 lines/mm was then applied on the polished sample at room temperature. This grating gives a sensitivity of 417 nm/fringe order. An epoxy material was used to adhere the grating to the sample. This epoxy material was allowed to cure for 48 h to ensure that the grating gets properly attached

Fig. 2 (a) Cross-sectioned sample before grating application. (b) Cross-sectioned sample after grating application



to the polished sample. The cross-section of the cut sample before and after applying the grating is shown in Fig. 2(a) and (b) respectively.

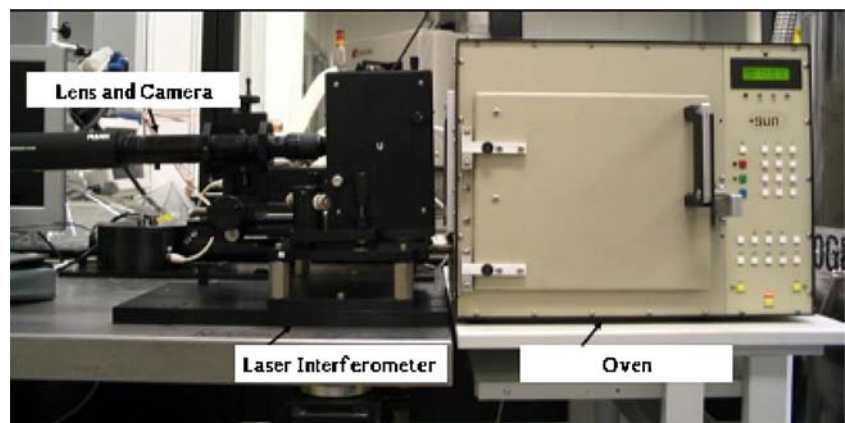
Experimental Setup

The laser moiré equipment from Photomechanics was used for this study. The experimental setup is shown in Fig. 3. The incident angle α of the laser beam shown in Fig. 1 can be precisely controlled for both the U and the V field laser beams using a vernier scale on the interferometer. The specimen with the moiré grating is placed on a holder that is attached directly to the moiré interferometer through a connecting rod. This arrangement ensures that the specimen moves along with the interferometer and thus ensuring that there is no relative movement of the specimen with respect to the interferometer. The specimen and the holder are then placed inside the thermal chamber maintained at atmospheric pressure. Before performing the experiment, the equipment needs to be calibrated for null fringes. This involves adjusting the incident angle α of the laser source for both the U and V field laser sources so that the reflected light is of -1 order i.e. it is perfectly normal to the surface. After calibration, the number of observed fringes is close to zero. The chamber has built-in heating coils which can be used to heat the chamber at a user specified heating rate to a temperature of up to 150°C. The deformation fringes on the grating observed due to temperature excursion can be captured in-situ using a lens and a CCD camera.

High Temperature Dwell

The moiré interferometry grating was applied and calibrated for null fringes at room temperature. This makes the room temperature a reference temperature with respect to which the deformation at a higher temperature will be measured. At higher temperature, the whole package deforms and U and V deformation fringe patterns are obtained. Since the package assembly is symmetric, only half of the package needs to be analyzed. Solder deformation at a given temperature and

Fig. 3 Moiré interferometry experimental setup

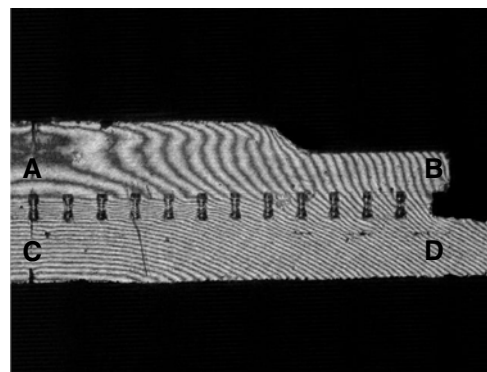


over a given period of time is governed by its creep behavior as well as the time-dependent deformation of the surrounding materials. Therefore, it is necessary to study the time-dependent deformation of the surrounding substrate and board prior to studying solder deformation. As a first step, we need to investigate the U and V deformation behavior of the substrate and board. Accordingly, two points—one at the center and one near the edge—were chosen to understand the relative U and V deformation of the substrate as well as the board.

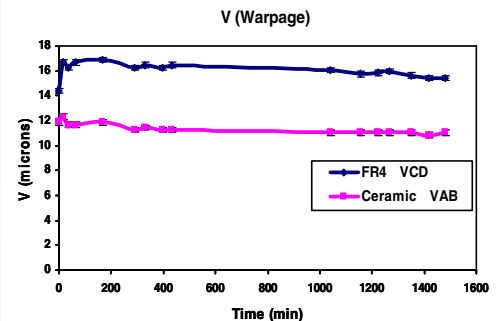
Warpage

As shown in Fig. 4(a), points A and B reside on the substrate and points C and D reside on the board. The warpage as a function of time was measured between points A and B for the ceramic substrate and between points C and D for the PWB board as shown in Fig. 4(a). ΔV_{AB} ($V_B - V_A$) represents the warpage of the substrate and ΔV_{CD} ($V_D - V_C$) represents the warpage of the PWB board. The warpage as a function of time is shown in Fig. 4(b). Since the fringes are manually counted, the error in measurement is equal half a fringe order. ΔV is positive for both the materials indicating that the whole assembly warps up. ΔV_{AB} is less than ΔV_{CD} indicating that the warpage of the ceramic is less than the warpage of the PWB board due to its higher modulus. If the assembly is maintained at 100°C for long duration, lasting

Fig. 4 (a) V -field displacement contours. (b) Warpage variation with time (the distance between points A and B is 25 mm)



(a)



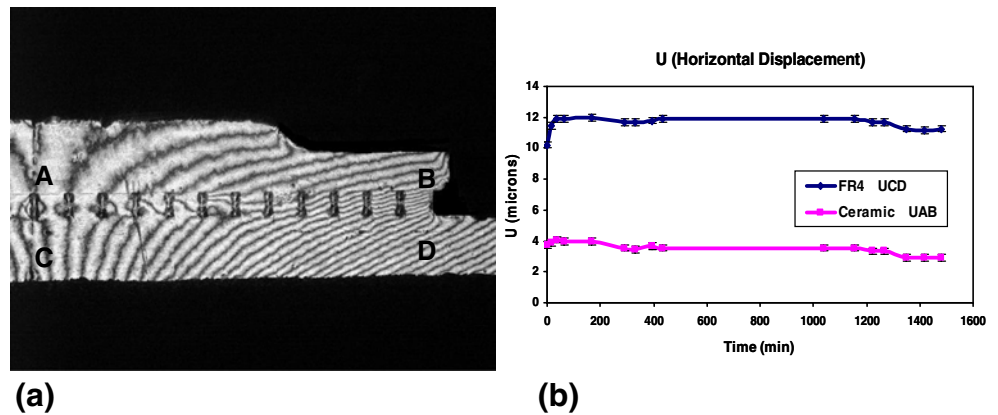
(b)

almost a day, the solder bump relaxes due to creep and provides less and less coupling between the substrate and the PWB board material. The warpage of the board and the substrate therefore decreases gradually with time. Prior to conducting the experiments, a sample was placed in the chamber with a thermocouple, and it was determined that it would take approximately 30 min for the sample to reach the chamber temperature. During this period the warpage increases slightly with time and this can be seen in Fig. 4(b).

Horizontal Displacement

The horizontal displacement contours are shown in Fig. 5(a). As the sample is heated, both ceramic and FR4 expand horizontally, although ceramic expansion is less than the expansion of FR4 due to its lower CTE. This is illustrated in Fig. 5(b) where ΔU ($U_B - U_A$ for the ceramic and $U_D - U_C$ for the FR4 board) is positive for both ceramic substrate and organic board. The magnitude of ΔU is roughly of the order of $L\alpha\Delta T$ which represents the unconstrained expansion length of the ceramic substrate and the board. Here, L is the distance between points AB (or CD), α is the CTE of the material considered and ΔT is the temperature difference between room temperature and 100°C . The unconstrained expansion length of the ceramic substrate and the PWB board is 6.6 and 15.7 μm respectively. However, as the ceramic

Fig. 5 (a) U -field displacement contours. (b) Horizontal displacement variation with time (the distance between points A and B is 25 mm)

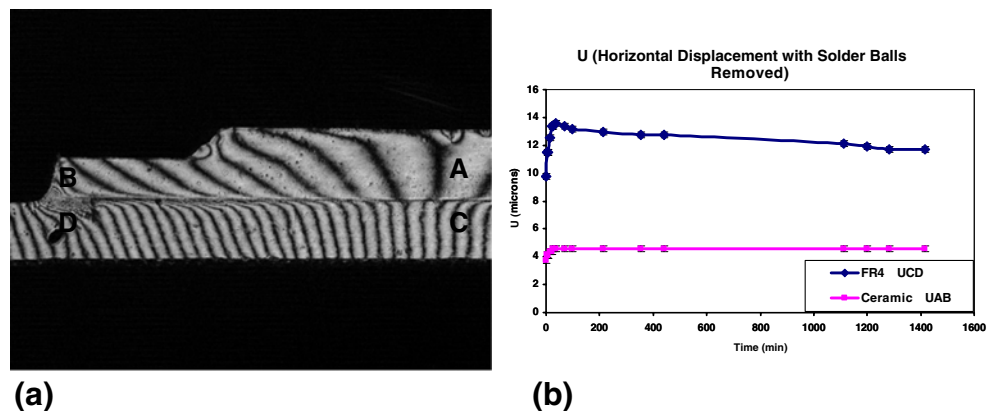


substrate and the board are coupled together with solder balls and as other materials are present in the package, we can use $L\alpha\Delta T$ only for an order-of-magnitude analysis.

As time progresses, the solder balls relax more and more and this reduces the coupling between the ceramic substrate and the PWB board. One would therefore expect the horizontal displacements of the ceramic substrate to decrease and the PWB board to increase. The horizontal displacements of both these materials were measured as a function of time between the points A and B in the ceramic substrate and C and D in the PWB board as shown in Fig. 5(b).

The horizontal displacement of the ceramic substrate decreases with time as expected. The horizontal displacement of the PWB however does not increase as expected. This can be attributed to the fact that the FR4 board being viscoelastic relaxes with time. The relaxation of the FR4 board causes its horizontal displacement to decrease. This competes with the increase in its length due to solder ball relaxation. To clearly observe the relaxation behavior of the FR4 board, the solder bumps were removed and the ceramic substrate was glued to the PWB board and the deformation of the assembly when maintained at 100°C was observed for 24 h. As shown in Fig. 6, the horizontal deformation of the PWB decreases with time due to relaxation. The ceramic substrate however maintains its constant length throughout the duration of the study.

Fig. 6 (a) U -field displacement contours. (b) Horizontal displacement variation with time (the distance between points A and B is 25 mm)



Carrier Fringe Implementation

Thus far, the horizontal and vertical displacements in locations close to top center and bottom center of the outermost solder joint have been obtained using laser moiré interferometry. Although such an information is helpful to understand the potential effect of substrate and board deformation and relaxation on solder deformation, it is necessary to study solder joint deformation in detail. Accordingly, this paper has used carrier fringes to be able to obtain solder joint local deformation contours with higher resolution.

Obtaining increased fringe counting accuracy from the moiré interferometry equipment using carrier fringes requires determining the phase of the fringes at a given location. The phase can be determined based on the fact that the Fourier transform of a high frequency fringe pattern is tri-modal in nature. The displacement fringes from the deformed specimen do not have the high frequency quality needed for it to be tri-modal. High frequency carrier fringes are therefore introduced which modulates the existing displacement pattern to make the Fourier transform of the net fringe pattern tri-modal. The net fringe pattern is due to the combination of the existing displacement pattern and the externally added high frequency carrier fringes with constant frequency. Phase information can then be easily extracted from the Fourier transformed image. The procedure is outlined below.

The intensity profile of the displacement fringes on the ceramic BGA sample, at a given point, when captured on a CCD camera has a form shown in equation (4) [20]:

$$I_{\alpha}(x,y) = I_b(x,y) + I_n(x,y) + I_o(x,y) \cos(\phi_{\alpha}(x,y))$$

$$\alpha = u \text{ for } U\text{-field}; \alpha = v \text{ for } V\text{-field} \tag{4}$$

where, $I_b(x,y)$ is the intensity due to background illumination, $I_n(x,y)$ is the intensity due to background noise, $I_o(x,y)$ is the amplitude of the fringe interferogram and $\phi_{\alpha}(x,y)$ is the phase of the displacement fringes. To obtain the phase of the displacement fringe pattern, the contributions due to background noise and illumination should be eliminated. As these two quantities are unknown, the equation (4) cannot be solved algebraically. However, the background illumination and noise have zero frequency. Fourier transform method can therefore be used as an alternate method to eliminate the background illumination and noise. The U -field and V -field fringe patterns and its Fourier transform is shown in Fig. 7(a) and (b). The contributions due to the background noise and the illumination are centered at the origin. The U and V -field displacement fringes have a finite frequency which varies with location. The average frequency however is dependent on the applied load and is typically not very high. As can be seen from Fig. 7(a) and (b) the contributions due to the displacement fringes in the Fourier transformed image is still located around the origin. Filtering out the background noise and illumination might lead to loss of data from the displacement fringe pattern.

Carrier fringes are introduced by a tiny adjustment of the angle α of the incident laser beam from the null calibration angle shown in Fig. 1. Carrier fringes are fringes having a constant frequency in either the U or V direction. The intensity profile of the fringes after introducing carrier fringes in the U and V field is given by equations (5) and (6) respectively [20]:

$$I_{cu}(x,y) = I_b(x,y) + I_n(x,y) + I_o(x,y) \cos(2\pi f_{cx}x + \phi_u(x,y))$$

$$\tag{5}$$

$$I_{cv}(x,y) = I_b(x,y) + I_n(x,y) + I_o(x,y) \cos(2\pi f_{cy}y + \phi_v(x,y))$$

$$\tag{6}$$

where, f_{cx} and f_{cy} are the carrier frequencies introduced in the x and y directions respectively and $\phi_u(x,y)$ and $\phi_v(x,y)$ represent the phase at given location for the U -field and the V -field. Equations (5) and (6) can be rearranged to equations (7) and (8) respectively as shown below.

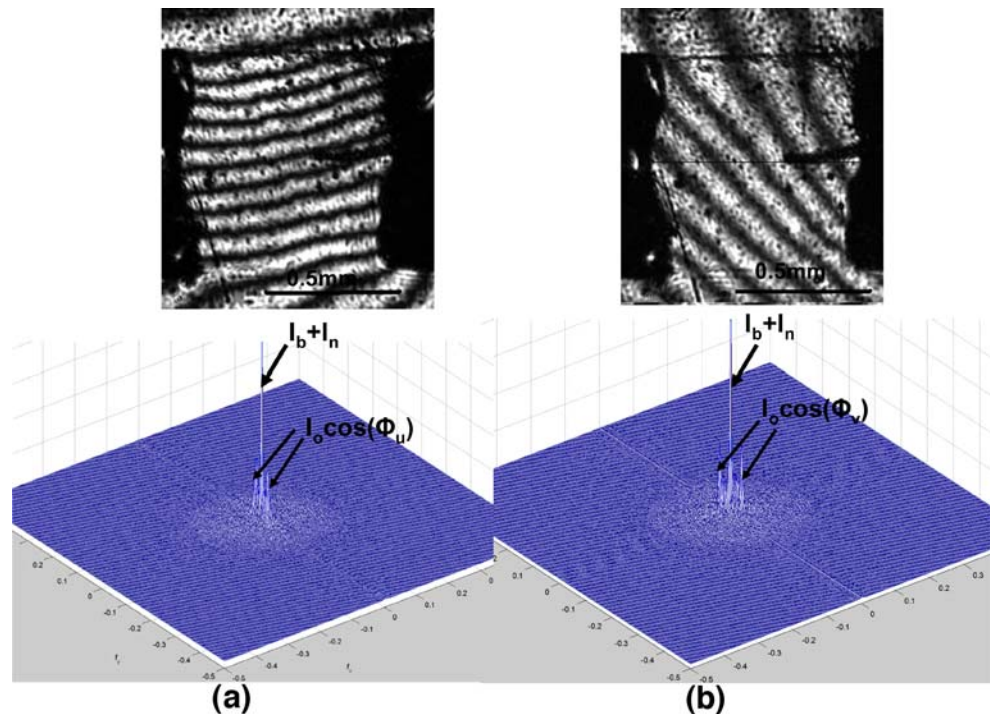
$$I_{cu}(x,y) = I_b(x,y) + I_n(x,y) + C_u(x,y)e^{2\pi i f_{cx}x}$$

$$+ C_u^*(x,y)e^{-2\pi i f_{cx}x} \tag{7}$$

$$I_{cv}(x,y) = I_b(x,y) + I_n(x,y) + C_v(x,y)e^{2\pi i f_{cy}y}$$

$$+ C_v^*(x,y)e^{-2\pi i f_{cy}y} \tag{8}$$

Fig. 7 (a) Fourier transform of U -field fringe pattern without carrier fringes. (b) Fourier transform of V -field fringe pattern without carrier fringes



where, $C_u(x,y)$ and $C_v(x,y)$ are given by:

$$C_u(x,y) = \frac{1}{2} I_o(x,y) e^{i\phi_u(x,y)} \tag{9}$$

$$C_v(x,y) = \frac{1}{2} I_o(x,y) e^{i\phi_v(x,y)} \tag{10}$$

The C_u^* and C_v^* represent the complement of C_u and C_v respectively. The Fourier transform of the equations (7) and (8) is given in equations (11) and (12) respectively.

$$I_{cu}(f_x, f_y) = I_{bn}(f_x, f_y) + C_u(f_x - f_{cx}, f_y) + C_u^*(f_x + f_{cx}, f_y) \tag{11}$$

$$I_{cv}(f_x, f_y) = I_{bn}(f_x, f_y) + C_v(f_x, f_y - f_{cy}) + C_v^*(f_x, f_y + f_{cy}) \tag{12}$$

where, f_x and f_y are the coordinates in the frequency domain. The first term in both the equations above represent contributions from the background illumination and the noise and is centered at the origin. The second and third term in the equations (11) and (12) are symmetric peaks with respect to the origin and centered around the respective carrier frequencies introduced. If the introduced carrier frequencies f_{cx} and f_{cy} are high enough the peaks due to displacement fringes encoded in the second and third term of equations (11) and (12) will be noticeably far from the

origin. The background noise and illumination can therefore be easily filtered. Moreover, since the peaks are symmetric around the origin, one of the peaks can be filtered out and the other peak can be moved by an amount equal to the frequency of the introduced carrier fringes to obtain $C_u(f_x, f_y)$ and $C_v(f_x, f_y)$. An inverse Fourier transform of these two quantities will give back the equations (9) and (10). Phase for the U and the V field can then be easily determined using the relation given in equations (13) and (14).

$$\phi_u(x,y) = \tan^{-1} \frac{\text{Im}(C_u(x,y))}{\text{Re}(C_u(x,y))} \tag{13}$$

$$\phi_v(x,y) = \tan^{-1} \frac{\text{Im}(C_v(x,y))}{\text{Re}(C_v(x,y))} \tag{14}$$

Once the phase information is obtained, the fringe counting accuracy of the U and V field fringe patterns can be increased n times by using the relations given in equations (15) and (16). These two relations are formulated based on the fact that the grey scale intensity displayed in an image varies between 0 to 255 [20].

$$I_u(x,y) = 127(1 + \cos(n\phi_u(x,y))) \tag{15}$$

$$I_v(x,y) = 127(1 + \cos(n\phi_v(x,y))) \tag{16}$$

Figures 8 and 9 illustrate the methodology for the U and V field fringe patterns in a solder ball where the fringe

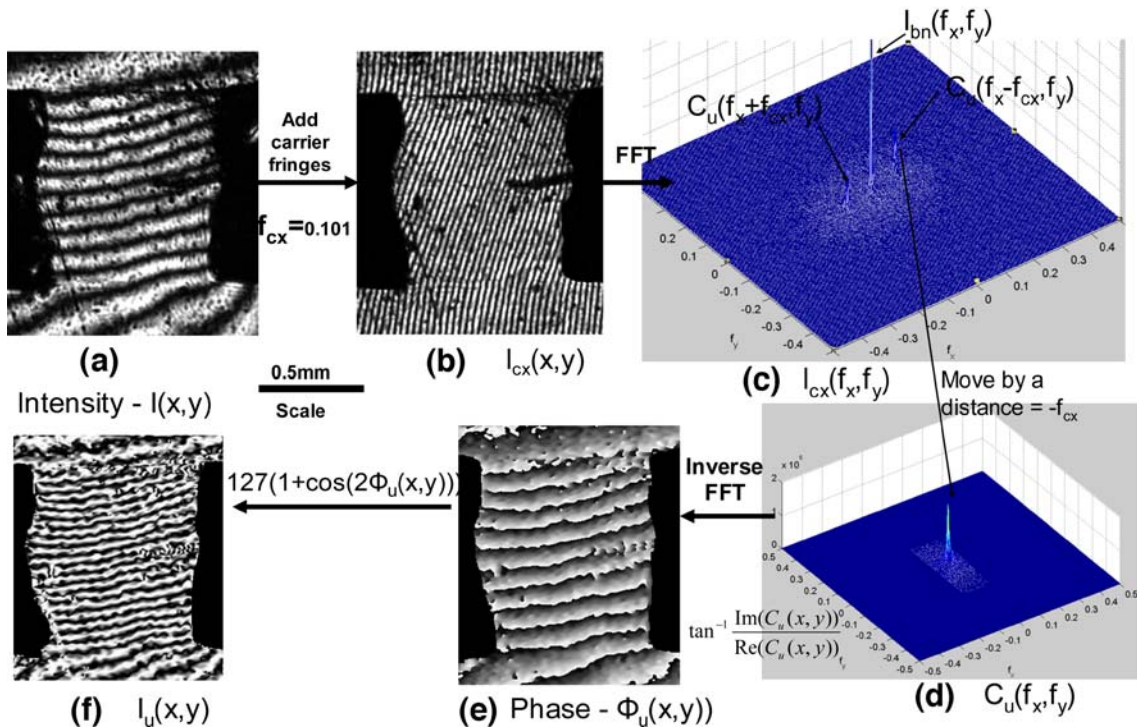


Fig. 8 Procedure for increasing the fringe counting accuracy in the U field

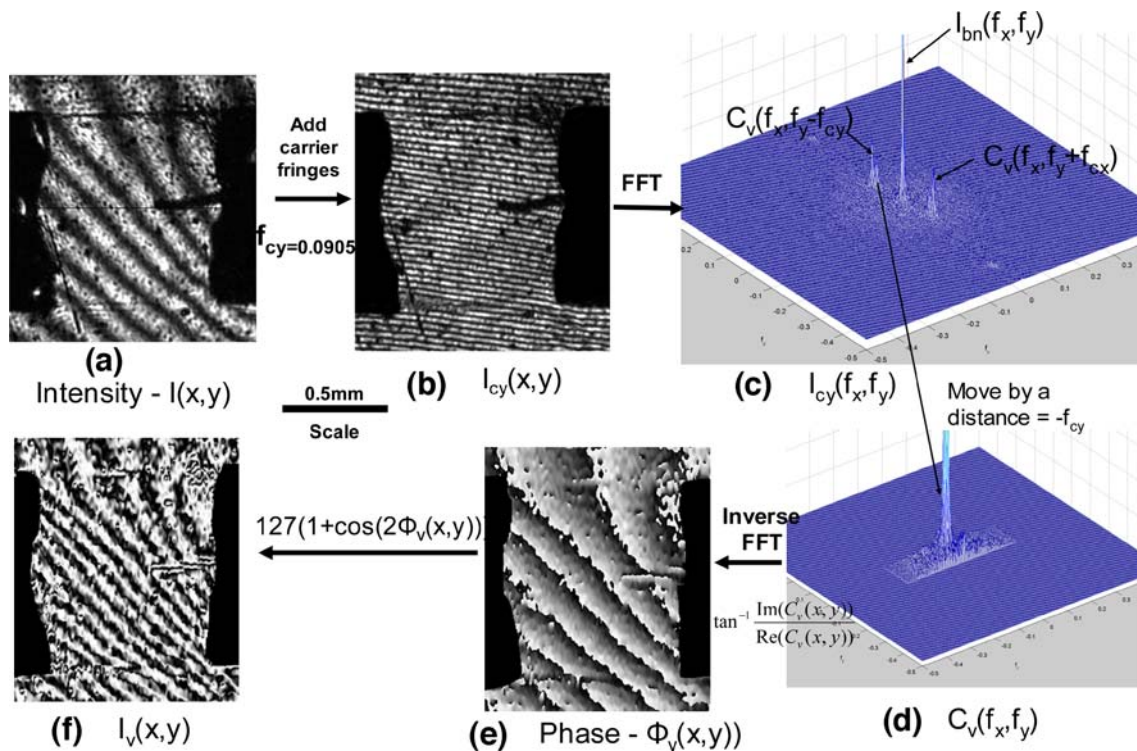


Fig. 9 Procedure for increasing the fringe counting accuracy in the V field

counting accuracy was increased by two times by introducing a carrier frequency of 0.101/pixel for the U -field and 0.0905/pixel for the V -field. A two fold increase in fringe counting accuracy was found to be sufficient for the present study. Figure 8(a) shows the fringe pattern as obtained from laser moiré interferometry. Figure 8(b) shows the image where the carrier fringes of constant frequency have been added to the deformed fringe pattern of varying frequency. Figure 8(c) shows the frequency domain plot obtained through FFT applied on Fig. 8(b). The horizontal axes represent the frequencies while the vertical axis shows the fringe intensity. As seen, the intensity is high at zero frequency indicating the background illumination and noise. The other two peaks correspond to the dominant frequency of the combined fringe pattern consisting of the deformed fringe pattern and the carrier fringe pattern. Figure 8(d) shows only the dominant frequency of the deformed fringe pattern after filtering out the background illumination and noise and after subtracting the carrier fringe pattern. Figure 8(e) shows the phase image obtained after taking the inverse FFT of Fig. 8(d). Using the phase image, Fig. 8(f) can be obtained where several fringe patterns are shown to interpolate between the existing fringe patterns shown in Fig. 8(a). Similar processing steps were carried out for Fig. 9 as well.

When the carrier fringes are added using laser moiré apparatus, the resulting image is shown in Fig. 8(b). The boundary contours of the solder joint are identical to the

boundary contours of the solder image in Fig. 8(a). As seen, the background image is dark while the solder image has the fringe pattern. However, after FFT processing, the carrier fringes are subtracted using software throughout the entire image consisting of the solder region and the background region. Such a subtraction leaves negative carrier fringe pattern in the background region which was originally dark. This background region with the negative carrier fringe pattern was subsequently masked through software to present the solder images in Fig. 8(e) and (f). The solder boundary used in such a masking process may not be identical to the solder boundary in Fig. 8(a) and (b), and thus the images in Fig. 8(e) and (f) appear to be distorted. In reality, if one were to be very careful with the background masking process, all of the solder images from Fig. 8(a) through (f) will remain identical.

The implemented carrier fringe technique is another way of improving fringe counting accuracy by introducing phase information to the fringes. As explained earlier, the carrier fringes of constant frequency are added and then subtracted to be able to get the phase information of the original fringe pattern. Using the phase information, several interpolating fringes can be obtained between the existing fringes. In the presented images, we have added one additional fringe between every two existing fringes. However, it is possible to add two or more of such additional fringes between two existing fringes. It should be pointed out such a technique contributes toward improving fringe counting accuracy, but not toward improving system sensitivity which is defined by the hardware.

Solder Strain Calculation

Solder strain computation was performed for the outermost solder ball in the laser moiré sample, as the outermost solder ball experiences the maximum strain in a CBGA package assembly. Manual fringe counting was done using the increased resolution displacement fringes obtained from the procedure outlined above to determine the average strains in the outermost solder ball. With a two-fold increase in fringe counting accuracy the average vertical normal strain, at a given temperature, in a solder joint are given by:

$$\varepsilon_{yy} = \frac{\partial v}{\partial y} = \frac{1}{2f} \left(\frac{\Delta N_y}{\Delta y} \right) \quad (17)$$

where, ΔN_y is the number of fringes observed in the solder ball in the y direction in the V field fringe pattern, and Δy is the standoff height of the solder ball (0.817 mm).

The average shear strain in a solder joint is given by:

$$\varepsilon_{xy} = \frac{1}{2} \left(\frac{\partial u}{\partial y} + \frac{\partial v}{\partial x} \right) = \frac{1}{4f} \left(\frac{\Delta N_x}{\Delta y} + \frac{\Delta N_y}{\Delta x} \right) \quad (18)$$

where, ΔN_x is the number of fringes observed in the solder ball in the x direction and Δx is the width of the solder ball (0.781 mm). The direction and the length along which the fringes were counted for the U -field and the V -field to evaluate the strains is indicated in Fig. 10.

Results and Discussion

The U and V field fringe patterns at 0 and 24 h before carrier fringe implementation are shown in Fig. 11(a) and (b) respectively. The U and V field fringe patterns at 0 and 24 h after carrier fringe implementation are shown in Fig. 11(c) and (d) respectively. The improvement gained in fringe counting accuracy can clearly be seen by comparing these two sets of figures. The U and V field fringe patterns changed during the course of 24 h. The U and V field

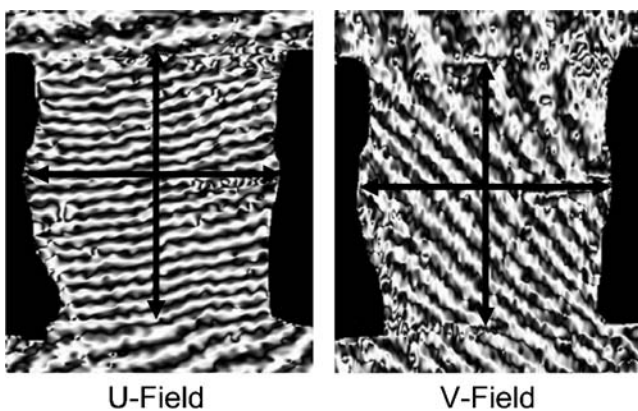


Fig. 10 Fringe counting direction

fringe patterns at the start and the end of dwell at 100°C are shown in Fig. 11. As it takes roughly 30 min for the package to reach the chamber temperature, the first image at time $t=0$ was taken after the temperature of the sample has reached the chamber temperature. It can be seen from Fig. 11(c) and (d) that the number and the direction of the fringes in both of the patterns have changed. The change is easily noticeable because of the increased density of the moiré fringe patterns.

Solder joint fringes were captured several times over the 24-h dwell at 100°C, fringes were counted, and strains were computed. Figure 12 shows the variation of shear and normal strains with time for the outermost solder joint. The error in fringe counting has reduced by half due to increased fringe counting accuracy obtained by carrier fringe implementation.

Variation of Shear Strains with Time during 100°C Dwell

The shear strain measured in a solder bump at a given instant of time is a combination of elastic strain, time-independent plastic strain and time-dependent creep strain. When the BGA package is exposed to 100°C, the CTE mismatch between the ceramic substrate and the PWB board causes the elastic strain and plastic strain to develop immediately. The value of the shear strains at time $t=0$ represents the contributions due to the above two components. As seen in Fig. 12, the shear strain continues to increase with time, and seems to stabilize after roughly 6 h. At 100°C, the homologous temperature of the solder alloy is greater than 0.5. The increase in shear strain at this temperature is due to the contribution of creep deformation behavior exhibited by the solder joint. With time, the solder joint relaxes more and more and the board and the substrate approach their unconstrained length. The driving force for solder shear deformation therefore decreases with time. This leads to a decrease in the rate of increase of shear strain with time. Beyond 6 h, the rate of increase of shear strain becomes very small and is hardly noticeable. The laser moiré interferometry fringes do not have sufficient resolution to capture such small increase in creep strain.

The du/dy component of the shear strain is directly related to the difference in the horizontal displacements of the top surface of the solder joint (adjoining the ceramic substrate) and the bottom surface of the solder joint (adjoining the PWB board) divided by the representative standoff height of the solder ball. The dv/dx component of the shear strain is related to the local variation of the bending (warp) of the ceramic substrate and the PWB board divided by the representative width of the solder ball. Both of these derivatives increase with time, although the rate of increase decreases with time. Therefore, the shear strain also increases with time with a decreasing rate, as shown in Fig. 12.

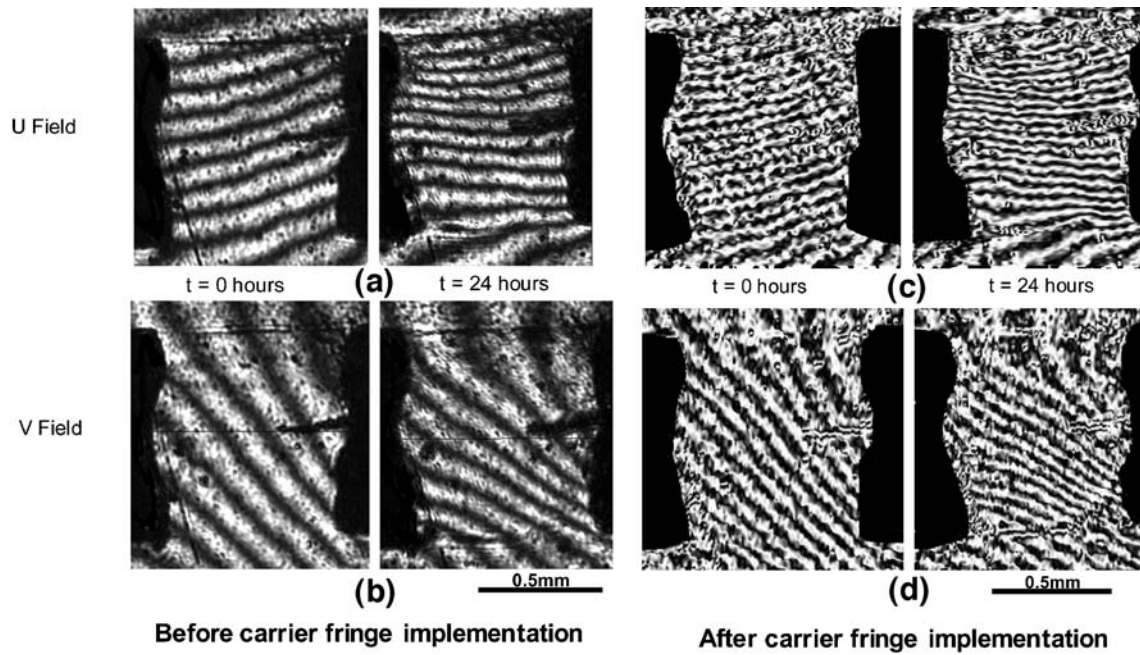


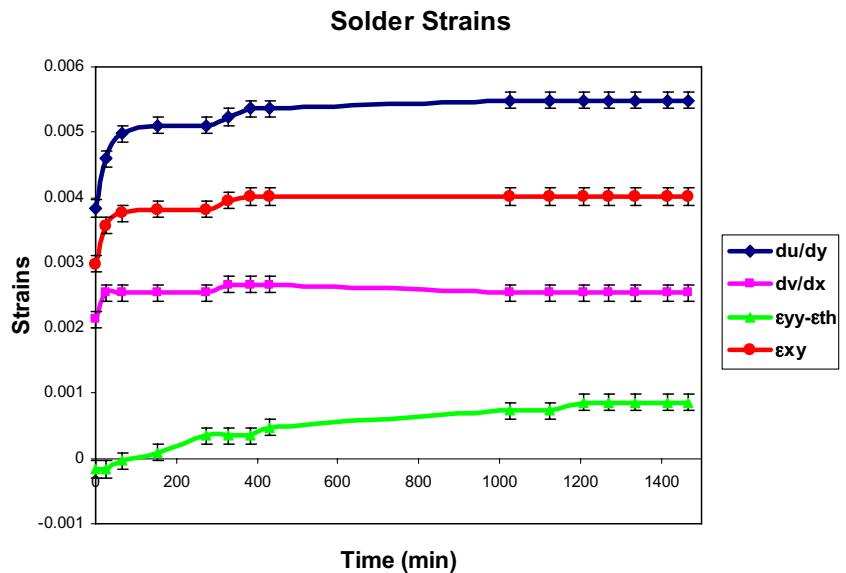
Fig. 11 (a) U field fringe pattern before and after dwelling at 100°C for 24 h. (b) V field fringe pattern before and after dwelling at 100°C for 24 h

Variation of Normal Strains with Time during 100°C Dwell

The normal strains in a solder joint is related to the difference in the warpage of the ceramic substrate and the PWB board at the region of the solder joint. The nature of the normal strains in the solder joint when cooled from higher temperature to lower temperature has been studied by Guo et al. [4]. They have shown that the normal strains in the vertical direction tend to be compressive at the center and gradually become less and less compressive for the solder joints away from the center. For the solder joints at the corner of the package, they have shown that the strains are tensile in nature. In our case, however, the fringe

contours and strains were obtained under heating, and thus the normal strains measured for the current ceramic BGA package showed compressive strains for the outermost solder joints as shown in Fig. 12. Increased warpage of the PWB board when compared to the ceramic substrate at the outermost solder joint location lead to compressive strains in that solder joint. It should be pointed out that the normal strain measured in the solder joints from moiré interferometry is a combination of thermal strain and mechanical strain. In Fig. 12, the thermal strain (ϵ_{th}) was subtracted prior to obtaining the normal mechanical strain ϵ_{yy} in the solder joint. The magnitude of the thermal strain is equal to $\alpha_{solder}\Delta T$.

Fig. 12 Variation of normal strains and shear strains as function of time



As the package is maintained at this temperature for longer duration, the warpage of the FR4 board and the ceramic substrate decreases with time due to solder ball creep relaxation. Added to this, the viscoelastic nature of PWB board causes it to relax more and reduce its warpage at a higher rate compared to the ceramic substrate. As a consequence, the normal strain in the outermost solder joint becomes less and less compressive. After about 100 min of dwell time, the normal strain becomes tensile in nature and the magnitude of the tensile strain increases with time.

Conclusions

Long-term high-temperature dwell behavior of solder interconnects is of interest to the electronic packaging community. Traditional laser moiré system requires expensive phase shifting apparatus to study minor changes in the deformation pattern under long-term dwell. This work has developed a method based on carrier fringes to study the long-term dwell behavior of solder joints at high temperature.

The deformation behavior of a ceramic BGA package when exposed to long dwell time lasting to 24 h duration was studied. The warpage and the horizontal displacement of the ceramic substrate and the PWB board as a function of time at a high temperature was determined using laser moiré interferometry with a sensitivity of 417 nm/fringe order. A Fourier transform method with carrier fringes was used to increase the fringe counting accuracy of the moiré interferometry system two fold. This method allows increasing the measurement resolution by a mere adjustment of the incident angle of the laser beams. Expensive phase shifting apparatus is not necessary. The strains in the small sized solder joints were estimated using this method.

The shear strain in the solder joint was found to increase due to solder joint creep relaxation. The relaxation of the solder joints with time lead to the decreased warpage of the ceramic substrate and the PWB board. The viscoelastic nature of the FR4 in the PWB substrate caused it to relax more than the ceramic substrate. The normal strains in the solder joints which was compressive initially changed to tensile after about 100 min of dwell time.

Acknowledgement This work was funded by the Army Research Lab, Raleigh, NC. We are thankful for their financial support for this research activity.

References

- Han B (2003) Thermal stresses in microelectronics subassemblies: quantitative characterization using photomechanics methods. *J Therm Stress* 26:583–613.
- Ham SJ, Lee SB (2003) Measurement of creep and relaxation behaviors of wafer-level CSP assembly using moiré interferometry. *J Electron Packag* 1252:282–288.
- Cho S, Han B, Joo J (2004) Temperature dependent deformation analysis of ceramic ball grid array package assembly under accelerated thermal cycling condition. *J Electron Packag* 1261:41–47.
- Guo Y, Lim CK, Chen WT, Woychik CG (1993) Solder ball connect (SBC) assemblies under thermal loading: I. Deformation measurement via moiré interferometry and its interpretation. *IBM J Res Develop* 375:635–646.
- Stout EA, Sottos NR, Skipor AF (2000) Mechanical characterization of plastic ball grid array package flexure using moiré interferometry. *IEEE Trans Adv Packaging* 234:637–645.
- Basaran C, Cartwright A, Zhao Y (2001) Experimental damage mechanics of microelectronics solder joints under concurrent vibration and thermal loading. *Int J Damage Mech* 102:153–170.
- Ye H, Basaran C, Hopkins DC, Lin M (2005) Modeling deformation in microelectronics BGA solder joints under high current density, Part I: simulation and testing. *Proceedings of the 55th Electronic Components and Technology Conference* 2:1437–1444.
- Post D, Han B, Ifju P (1994) *High sensitivity moiré*. Springer, New York.
- Guo Y, He X, Zou D, Liu S (1998) Phase-shifting analysis in moiré interferometry and its applications in electronic packaging. *Opt Eng* 375:1410–1419.
- Wang Z, Han B (2004) Advanced iterative algorithm for phase extraction of randomly phase-shifted interferograms. *Opt Lett* 2914:1671–1673.
- Heng L, Cartwright AN, Basaran C (2004) Moiré interferogram phase extraction: a ridge detection algorithm for continuous wavelet transforms. *Appl Opt* 43:850–857.
- Guo Y, Han B (1995) Thermal deformation analysis of various electronic packaging products by moiré and microscopic moiré interferometry. *J Electron Packag* 1173:185–191.
- Guo Y, Post D, Czarnek R (1989) The magic of carrier fringes in moiré interferometry. *Exp Mech* 292:169–173.
- Nicola SD, Ferraro P (2000) Fourier transform method of fringe analysis for moiré interferometry. *J Opt A Pure Appl Opt* 2:228–233.
- Han B, Post D (1989) The tilted plate method for introducing carrier fringes of extension in moiré interferometry. *Exp Tech* 137:25–29.
- Choi HC, Guo Y, LaFontaine W, Lim CK (1993) Solder Ball Connect (SBC) assemblies under thermal loading: II. Strain analysis via image processing, and reliability considerations. *IBM J Res Develop* 375:649–659.
- Takeda M, Ina H, Kobayashi S (1982) Fourier-transform method of fringe-pattern analysis for computer-based topography and interferometry. *J Opt Soc Am* 721:156–160.
- Han B, Guo Y (1995) Thermal deformation analysis of various electronic packaging products by moiré and microscopic moiré interferometry. *J Electron Packag* 117:185–189.
- Dai F, McKelvie J, Post D (1990) An interpolation of moiré interferometry from wavefront interference theory. *Opt Lasers Eng* 12:101–118.
- Bhat G, Sciammarella CA (1991) Computer assisted techniques to evaluate fringe patterns. *Proceedings of SPIE, Laser Interferometry IV: Computer-Aided Interferometry* 1553:252–262.